The Astrophysical Journal, 898:50 (9pp), 2020 July 20 https://doi.org/10.3847/1538-4357/ab9808

Bremsstrahlung in GRMHD Models of Accreting Black Holes

Ricardo Yarza[1,2], George N. Wong[1], Benjamin R. Ryan[3], and Charles F. Gammie[1,2]
[1] Department of Physics, University of Illinois, 1110 West Green Street, Urbana, IL 61801, USA; ricardo9@illinois.edu
[2] Department of Astronomy, University of Illinois, 1002 West Green Street, Urbana, IL 61801, USA
[3] CCS-2, Los Alamos National Laboratory, P.O. Box 1663, Los Alamos, NM 87545, USA
Received 2020 April 13; revised 2020 May 26; accepted 2020 May 28; published 2020 July 22

Abstract

The role of bremsstrahlung in the emission from hot accretion flows around slowly accreting supermassive black holes is not thoroughly understood. In order to appraise the importance of bremsstrahlung relative to other radiative processes, we compute spectral energy distributions (SEDs) of accretion disks around slowly accreting supermassive black holes including synchrotron radiation, inverse Compton scattering, and bremsstrahlung. We compute SEDs for (i) four axisymmetric radiative general relativistic magnetohydrodynamics (RadGRMHD) simulations of $10^8 M_\odot$ black holes with accretion rates between $10^{-8}\dot{M}_{\rm Edd}$ and $10^{-5}\dot{M}_{\rm Edd}$, (ii) four axisymmetric RadGRMHD simulations of M87* with varying dimensionless spin a_* and black hole mass, and (iii) a 3D GRMHD simulation scaled for Sgr A*. At $10^{-8}\dot{M}_{\rm Edd}$, most of the luminosity is synchrotron radiation, while at $10^{-5}\dot{M}_{\rm Edd}$ the three radiative processes have similar luminosities. In most models, bremsstrahlung dominates the SED near 512 keV. In the M87* models, bremsstrahlung dominates this part of the SED if $a_* = 0.5$, but inverse Compton scattering dominates if $a_* = 0.9375$. Since scattering is more variable than bremsstrahlung, this result suggests that 512 keV variability could be a diagnostic of black hole spin. In the Appendix, we compare some bremsstrahlung formulae found in the literature.

Unified Astronomy Thesaurus concepts: Accretion (14); Low-luminosity active galactic nuclei (2033); Radiative processes (2055); Supermassive black holes (1663); Radiative transfer (1335)

1. Introduction

Black holes with dimensionless accretion rate[4] $\dot{m} \equiv \dot{M}/\dot{M}_{\rm Edd} \leqslant 10^{-3}$ are thought to accrete through optically thin, geometrically thick, radiatively inefficient accretion flows (for a review, see Yuan & Narayan 2014). The dominant emission processes in these flows are synchrotron radiation and bremsstrahlung, and photons emitted by these processes may then be upscattered by inverse Compton scattering. Each of these processes has been extensively considered in the accretion flow literature (e.g., Narayan & Yi 1995; Esin et al. 1996; Mahadevan 1997), but bremsstrahlung is sometimes neglected because synchrotron radiation is energetically dominant at low accretion rates.

The effect of radiative processes on flow dynamics depends on $\dot{m}$. At very low $\dot{m}$, the plasma radiates only a negligible fraction of its internal energy before being accreted by the central black hole. Using numerical simulations, Dibi et al. (2012) found that radiative processes are negligible to the flow dynamics if $\dot{m} \leqslant 10^{-7}$. Another study (Ryan et al. 2017) found this constraint to be $\dot{m} \leqslant 10^{-6}$ instead, and attributed the difference to their electron temperature prescription (Ressler et al. 2015). As $\dot{m}$ increases, radiative cooling becomes increasingly important, motivating relativistic radiation magnetohydrodynamics (RadGRMHD) models of the flow. As we shall see, bremsstrahlung becomes increasingly energetically important compared to synchrotron radiation as $\dot{m}$ increases.

Even when the accretion rate is sufficiently low that radiative cooling is unimportant, photons produced at $h\nu \gtrsim m_e c^2$ may still dominate electron–positron pair production (Mościbrodzka et al. 2011; G. N. Wong et al. 2020, in preparation). Pairs created by background photon collisions can influence the structure of the accretion flow in regions where the native plasma density is too low to screen the electric field in the plasma frame, i.e., when the density is less than the Goldreich & Julian (1969) density. Therefore, even when bremsstrahlung is energetically negligible, it may still dominate the X-ray and gamma-ray radiation field and affect observables via pair production. Accurately accounting for the bremsstrahlung component of the radiation field may be important in future particle kinetics simulations (Ford et al. 2018; Parfrey et al. 2019) and magnetohydrodynamic models of pair production.

The structure of low-$\dot{m}$ black hole accretion flows is of particular interest with the advent of resolved millimeter-wavelength images of the black hole at the center of the elliptical galaxy M87 (Event Horizon Telescope Collaboration et al. 2019a; the black hole is hereafter referred to as M87*). X-ray observations of M87* are numerous (Böhringer et al. 2001; Wilson & Yang 2002; Di Matteo et al. 2003; Prieto et al. 2016; Event Horizon Telescope Collaboration et al. 2019b). Measuring M87*'s mass from gas dynamics yields $m \equiv M/M_\odot = 3.5 \times 10^9$ (Walsh et al. 2013), from stellar dynamics $m = 6.6 \times 10^9$ (Gebhardt et al. 2011), and from interferometric measurements $m = 6.5 \times 10^9$ (Event Horizon Telescope Collaboration et al. 2019c). The distance to M87* is approximately $D = 16.8$ Mpc (Blakeslee et al. 2009; Bird et al. 2010; Cantiello et al. 2018). Estimates and analysis of simulations show that $\dot{m} \sim 10^{-5}$ and that the dimensionless spin ($a_* \equiv Jc/GM^2$, where J is the angular momentum of the black hole) satisfies $|a_*| \gtrsim 0.5$ (e.g., Event Horizon Telescope Collaboration et al. 2019b).

Similarly, resolved millimeter-wavelength images of Sgr A* are expected in the near future. Sgr A*'s quiescent state has also been observed extensively in the X-ray (Baganoff et al. 2003; Bélanger et al. 2006; Nowak et al. 2012). Stellar orbit observations suggest $m = 4.05 \times 10^6$ (Boehle et al. 2016)

[4] $\dot{M}_{\rm Edd} \equiv 4\pi GM\, m_p/\eta\, \sigma_T c$, where $M \equiv$ black hole mass, $m_p \equiv$ proton mass, $\sigma_T \equiv$ Thompson cross section, and $\eta \equiv$ nominal efficiency, conventionally taken to be 0.1.

Table 1
Summary of the Three Sets of Simulations Used in This Work

Set Label	m	$\langle \dot{m} \rangle$	a_*	T_p/T_e
R	10^8	1.1×10^{-8}	0.5	N/A
		1.2×10^{-7}		
		9.3×10^{-7}		
		1.0×10^{-5}		
M87*	3.3×10^9	2.2×10^{-5}	0.5	N/A
		8.2×10^{-6}	0.9375	
	6.2×10^9	9.2×10^{-6}	0.5	
		5.2×10^{-6}	0.9375	
Sgr A*	4.05×10^6	1.4×10^{-8}	0.9375	1
		4.0×10^{-8}		3
		6.4×10^{-7}		10

Note. The first two sets are axisymmetric RadGRMHD `ebhlight` simulations. The third is a 3D GRMHD `harm` simulation scaled for Sgr A*. For more information about the first set (labeled R), see Ryan et al. (2017), and for the second set (labeled M87*), see Ryan et al. (2018).

and $D = 8.18$ kpc (Gravity Collaboration et al. 2019). Analysis of polarized radiation at $\lambda = 1.3$ mm (Marrone et al. 2006) suggests that the accretion rate at $r = 20GM/c^2$ is in the range $2 \times 10^{-9} \leqslant \dot{m} \leqslant 2 \times 10^{-7}$, and some GRMHD simulations (e.g., Mościbrodzka et al. 2009) find that $\dot{m} \sim 10^{-8}$ reproduces the observed 230 GHz flux (Marrone et al. 2006). At such low accretion rates, radiative cooling is negligible.

These considerations motivate a study of bremsstrahlung in low-$\dot{m}$ black holes. The recent development of RadGRMHD codes (e.g., Sądowski et al. 2014; Ryan et al. 2015) enables self-consistent studies of radiative cooling at accretion rates up to $\dot{m} \sim 10^{-5}$, which permits a more accurate evaluation of the importance of bremsstrahlung.

In this paper, we consider eight RadGRMHD models of accreting black holes and one nonradiative GRMHD model for Sgr A* (see Table 1 for a summary of the simulations). We compute their spectral energy distributions (SEDs) using a modified version of the radiative transfer code `grmonty` (Dolence et al. 2009) that includes synchrotron radiation, inverse Compton scattering, and bremsstrahlung. We study the relative importance of these radiative processes across several accretion rates and black hole spins, and discuss the SEDs computed for M87* and Sgr A*.

The paper is structured as follows: in Section 2, we describe the relevant equations and numerical methods, particularly the implementation of bremsstrahlung in `grmonty`. In Section 3, we discuss the importance of bremsstrahlung for various accretion rates for the axisymmetric RadGRMHD simulations. We then present the computed SEDs for M87* and Sgr A*, and compare them to observations. We conclude with final remarks and possibilities for future work in Section 4. In Appendices A through C, we briefly review some bremsstrahlung formulae found in the literature. We compare some of these formulae in Appendix D.

2. Techniques

The radiative transfer calculation is done by post-processing the fluid calculation. Both calculations assume that the plasma is composed of ionized hydrogen, is charge-neutral, and has a thermal electron velocity distribution. Here, we define the emission coefficient j_ν as the power emitted per unit volume per unit frequency per unit solid angle, and the cooling rate Λ as the power emitted per unit volume.

The fluid data were produced using two different codes: `ebhlight` and `harm`. `ebhlight` evolves the RadGRMHD equations with frequency-dependent radiative transfer, including the effects of synchrotron radiation and inverse Compton scattering. `ebhlight` is an extension of `bhlight` (Ryan et al. 2015) that tracks electron and ion temperatures independently according to the electron thermodynamics model of Ressler et al. (2015), and uses the Howes (2010) turbulent cascade model for electron heating. Both `bhlight` and `ebhlight` are based on the GRMHD code `harm` (Gammie et al. 2003) and the radiative transfer code `grmonty` (Dolence et al. 2009).

We use three sets of fluid simulations of standard and normal evolution (SANE; Narayan et al. 2012) accretion disks. The first set (Ryan et al. 2017, labeled R) contains four axisymmetric RadGRMHD `ebhlight` simulations. All of them have $m = 10^8$ and $a_* = 0.5$, but their time-averaged accretion rates $\equiv \langle \dot{m} \rangle$ are different and range from $\langle \dot{m} \rangle \approx 10^{-8}$ to $\langle \dot{m} \rangle \approx 10^{-5}$. These accretion rates cover the regime where radiative processes become relevant to the flow dynamics.

The second set (Ryan et al. 2018, labeled M87*) contains four axisymmetric RadGRMHD `ebhlight` simulations of M87*, corresponding to the four possible combinations of two masses ($m = 3.3 \times 10^9$ and $m = 6.2 \times 10^9$) and two spins ($a_* = 0.5$ and $a_* = 0.9375$). For each simulation, the accretion rate is such that the flux density at 230 GHz matches the observed value (Doeleman et al. 2012).

Both sets of `ebhlight` simulations used axisymmetrized 3D GRMHD simulation data as initial conditions. This procedure alleviates some limitations of axisymmetry, such as the long integration times required to achieve viscous electron heating equilibrium at larger radii. The SEDs obtained from these simulations are then time-averaged between $t = 600GM/c^3$ and $t = 1000GM/c^3$ with a $5GM/c^3$ cadence.

The third set (labeled Sgr A*) contains a 3D GRMHD `harm` simulation scaled for Sgr A* ($m = 4.05 \times 10^6$, $a_* = 0.9375$). The GRMHD simulation assumes a single fluid temperature, and then the radiative transfer calculation assigns a fixed temperature ratio between protons and electrons ($\equiv T_p/T_e$). Here we consider three values for this ratio (1, 3, and 10). We compute SEDs at an observing angle of $\pi/3$ and then time average between $t = 2000GM/c^3$ and $t = 10^4GM/c^3$ with a $100GM/c^3$ cadence. For every value of T_p/T_e, we normalize the GRMHD model so that the time-averaged 230 GHz flux in our SEDs matches the observed 2.4 Jy (Doeleman et al. 2008) to within ~1%.

Table 1 shows a summary of all simulations.

The fluid data from these simulations are post-processed using `grmonty` (Dolence et al. 2009), a relativistic Monte Carlo radiative transfer code. The code computes an SED from a single time slice of the fluid data using the "fast light" approximation, i.e., propagating photons through the computational domain while the fluid variables are held constant in time. The code accounts for synchrotron radiation, inverse Compton scattering, and bremsstrahlung (see Section 2.1). In addition to the total SED, `grmonty` records the SED produced by each radiative process individually. Photons produced by synchrotron or bremsstrahlung that get scattered as they propagate through the plasma are marked as inverse Compton scattering photons.

2.1. Bremsstrahlung

We consider bremsstrahlung emission from electron–ion and electron–electron encounters in an ionized hydrogen plasma. Fitting formulae for the bremsstrahlung cooling rate (Svensson 1982) show that in the high temperature limit, electron–electron bremsstrahlung contributes two-thirds of the total emitted power, i.e., $\Lambda^{\rm br,ee}/\Lambda^{\rm br,ei} = 3F_{\rm ee}(\Theta_{\rm e})/(8\pi F_{\rm ei}(\Theta_{\rm e})) \sim 2$. Here $\Theta_{\rm e} \equiv k_{\rm B} T_{\rm e}/m_{\rm e}c^2$ is the dimensionless electron temperature, where $T_{\rm e} \equiv$ electron temperature, $k_{\rm B} \equiv$ Boltzmann constant, $m_{\rm e} \equiv$ electron mass, and $c \equiv$ speed of light. The functions $F_{\rm ee}(\Theta_{\rm e})$ and $F_{\rm ei}(\Theta_{\rm e})$ are given in Stepney & Guilbert (1983) and reproduced in Appendices A and B. From these formulae, the temperature at which both types of bremsstrahlung have the same cooling rate is $\Theta_{\rm e} \sim 0.67$. The space-averaged $\Theta_{\rm e}$ in the simulations used here is of order unity, so electron–electron bremsstrahlung should be taken into account. The emission from outside the simulation domain ($r > 200GM/c^2$) is neglected.

Many bremsstrahlung emission coefficient formulae exist in the literature. The appendices summarize and compare some of these. For electron–ion bremsstrahlung, `grmonty` uses the emission coefficient (see, e.g., Rybicki & Lightman 1979)

$$j_\nu^{\rm br,ei} = \frac{8\, q_{\rm e}^6}{3\, m_{\rm e}^2 c^4}\sqrt{\frac{2\pi}{3}}\,\Theta_{\rm e}^{-1/2}\, n_{\rm e} n_i e^{-h\nu/k_{\rm B}T_{\rm e}}\bar{g}_{\rm ff}^{\rm ei}, \quad (1)$$

where $q_{\rm e} \equiv$ elementary charge, $n_{\rm e} \equiv$ electron number density, $n_{\rm i} \equiv$ ion number density, $h \equiv$ Planck constant, and $\bar{g}_{\rm ff}^{\rm ei}$ is the thermally averaged electron–ion Gaunt factor given as tabulated values in van Hoof et al. (2015). This Gaunt factor combines an exact nonrelativistic calculation (van Hoof et al. 2014) with a relativistic calculation in the Born approximation, thus spanning a large parameter space accurately. `grmonty` interpolates these values using $T_{\rm e}$ and ν as independent variables. For electron–electron bremsstrahlung, `grmonty` uses the emission coefficient of Nozawa et al. (2009),

$$j_\nu^{\rm br,ee} = \frac{4\pi\, q_{\rm e}^6}{3\, m_{\rm e}^2 c^4}\,\Theta_{\rm e}^{1/2}\, n_{\rm e}^2 e^{-h\nu/k_{\rm B}T_{\rm e}}\bar{g}_{\rm ff}^{\rm ee}, \quad (2)$$

where $\bar{g}_{\rm ff}^{\rm ee}$ is the thermally averaged electron–electron Gaunt factor given in Nozawa et al. (2009) as a piecewise fitting formula. This formula combines a nonrelativistic calculation (Itoh et al. 2002) with calculations where relativistic effects and/or Coulomb corrections are important. When `grmonty` encounters points in parameter space that are outside the domains of these two numerical calculations, it uses the nearest point inside the domains. These points are rare, and the spectrum is mostly insensitive to the way they are handled. We use Kirchhoff's law to account for bremsstrahlung absorption.

3. Results

We report quantities that have been time-averaged (the time average of f is denoted by $\langle f \rangle$) over the interval when the disk is in statistical steady state. In Section 3.1, we discuss general results about bremsstrahlung as a function of accretion rate. In Section 3.2, we show computed SEDs for M87* and Sgr A* and compare them to observations.

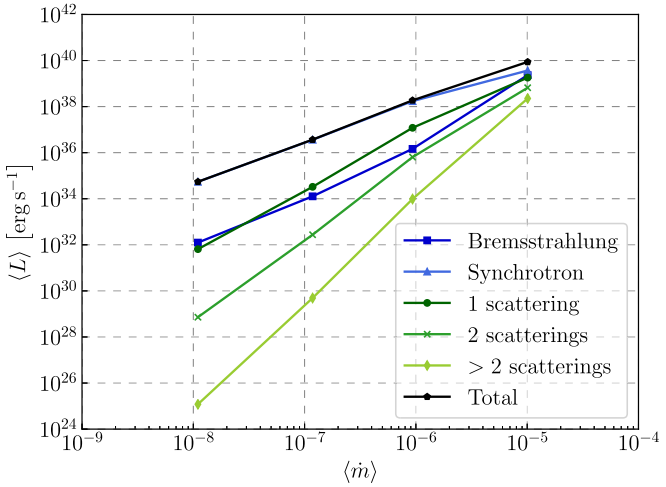

Figure 1. Time-averaged total luminosity for each radiative process in model set R ($m = 10^8$, $a_* = 0.5$) as a function of accretion rate. While synchrotron radiation dominates at lower accretion rates, bremsstrahlung and inverse Compton scattering become increasingly important as the accretion rate increases.

3.1. Bremsstrahlung as a Function of $\dot{m}$

Figure 1 shows the time-averaged total luminosity produced by each radiative process as a function of accretion rate for the models in set R. Synchrotron produces most of the luminosity at low accretion rates by a few orders of magnitude, but other radiative processes become increasingly important as the accretion rate increases. At $\langle \dot{m} \rangle \approx 10^{-5}$, synchrotron, bremsstrahlung, and inverse Compton scattering produce about 40%, 30%, and 30% of the total luminosity, respectively.

The ratio of bremsstrahlung and synchrotron luminosities scales roughly as $\Lambda^{\rm br}/\Lambda^{\rm synch} \propto n_{\rm e}^2\,\Theta_{\rm e}/(n_{\rm e}B^2\,\Theta_{\rm e}^2) = n_{\rm e}/(B^2\,\Theta_{\rm e})$, which is constant in the low-$\dot{m}$ limit (because $n_{\rm e} \propto \dot{m}$, $B \propto \dot{m}^{1/2}$, $\Theta_{\rm e}$ constant). Between our $\langle \dot{m} \rangle \approx 10^{-8}$ and $\langle \dot{m} \rangle \approx 10^{-7}$ simulations, the ratio between the bremsstrahlung and synchrotron luminosities increases by a factor of 1.5. In contrast, between $\langle \dot{m} \rangle \approx 10^{-6}$ and $\langle \dot{m} \rangle \approx 10^{-5}$, this ratio increases by a factor of 75, which shows that bremsstrahlung is becoming more important as the accretion rate increases. The ratio changes partly because the synchrotron luminosity scales subquadratically with $\langle \dot{m} \rangle$. Most synchrotron radiation is produced in the inner part of the disk, and in our models, electrons in this region are colder at higher $\langle \dot{m} \rangle$ (Ryan et al. 2017). Additionally, the scaling of the bremsstrahlung luminosity with $\langle \dot{m} \rangle$ changes slightly at $\langle \dot{m} \rangle \approx 10^{-6}$ as the effect of radiation on flow dynamics becomes significant. For $\langle \dot{m} \rangle \leqslant 10^{-6}$, the bremsstrahlung luminosity agrees with the low-$\dot{m}$ scaling, i.e., $\langle L^{\rm br} \rangle \propto \langle \dot{m} \rangle^2$. However, when $\langle \dot{m} \rangle \geqslant 10^{-6}$, the bremsstrahlung luminosity scaling changes to approximately $\langle L^{\rm br} \rangle \propto \langle \dot{m} \rangle^3$. This change in scaling is at least partially caused by increasing Coulomb heating of electrons at $r \gtrsim 15GM/c^2$ as the accretion rate increases (Ryan et al. 2017). In our models, as a consequence of the limited extent of the disk, the bremsstrahlung cooling rate peaks at $r \sim 40GM/c^2$. While thermal equilibrium is a concern here, we find that near the spatial peak of the bremsstrahlung cooling rate $\sigma_{\Theta_{\rm e}}/\langle \Theta_{\rm e} \rangle \lesssim 0.1$, where σ represents the standard deviation in time. Finally, the bremsstrahlung absorption optical depth near the peak frequency $\sim 10^{20}$ Hz is very small, so photons near the peak frequency can escape almost freely at all accretion rates.

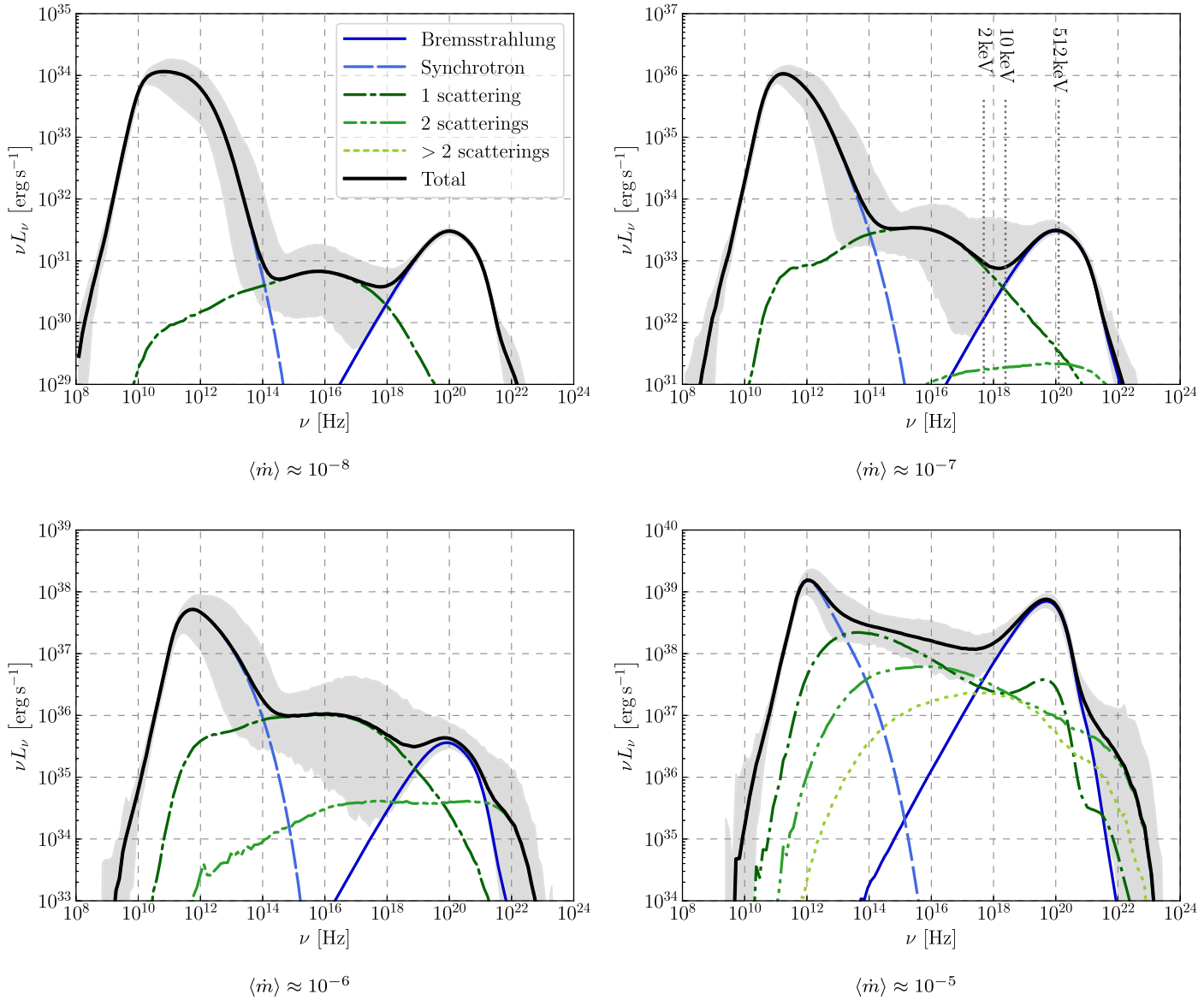

Figure 2. Time-averaged spectral energy distributions (SEDs) for the set R models ($m = 10^8$, $a_* = 0.5$). Each panel corresponds to one accretion rate. The shaded region around the total SED shows the variability throughout the time-averaging period. Bremsstrahlung dominates the SED near $\nu \sim 10^{20}$ Hz ($h\nu \sim 512$ keV) at all accretion rates.

Figure 2 shows the computed SEDs as a function of accretion rate for models in set R. Bremsstrahlung dominates the SED around $\nu \sim 10^{20}$ Hz at all accretion rates. However, the relative importance of bremsstrahlung and inverse Compton scattering is sensitive to at least black hole spin (see Section 3.2). The computed bremsstrahlung luminosity near the peak (between 10^{18} and 10^{21} Hz) satisfies $\sigma_L/\langle L \rangle \sim 0.1$ for all accretion rates. On the other hand, inverse Compton scattering has $\sigma_L/\langle L \rangle \sim 1$ at all accretion rates except at $\langle \dot{m} \rangle \approx 10^{-5}$, where $\sigma_L/\langle L \rangle \sim 0.5$.

3.2. M87* and SgrA*

Figure 3 shows the computed SEDs for M87*, as well as X-ray observations (Di Matteo et al. 2003; Prieto et al. 2016; Wong et al. 2017). These observations measured flux density with an aperture radius of 0.″4, which means they exclude emission from the jet at larger scales. Assuming a distance $D = 16.7$ Mpc to M87*, they captured the emission from a region of radius $\sim 10^5 GM/c^2$, which is considerably larger than $200GM/c^2$, the outer radius of our simulations. Although most of the emission comes from the inner region of the accretion flow, this discrepancy in simulation and observation sizes means the observations should be interpreted as upper limits.

At $a_* = 0.5$, bremsstrahlung dominates the SED near $\nu \sim 10^{20}$ Hz, in agreement with the results from model R. However, when $a_* = 0.9375$, the upscattered synchrotron photons dominate this part of the SED, and the bremsstrahlung peak is approximately one order of magnitude below. Accordingly, when $a_* = \{0.5, 0.9375\}$, bremsstrahlung contributes $\sim\{20\%, 1\%\}$ of the total luminosity. This difference between low and high spin models arises from their different temperature and density profiles. For all M87* models, the bremsstrahlung variability $\sigma_L/\langle L \rangle \sim 0.2$, while $\sigma_L/\langle L \rangle \sim 0.7$ for second order inverse Compton scattering. Since inverse Compton scattering is much more variable and dominates when $a_* = 0.9375$, these results suggest that variability near $\nu \sim 10^{20}$ Hz could be a

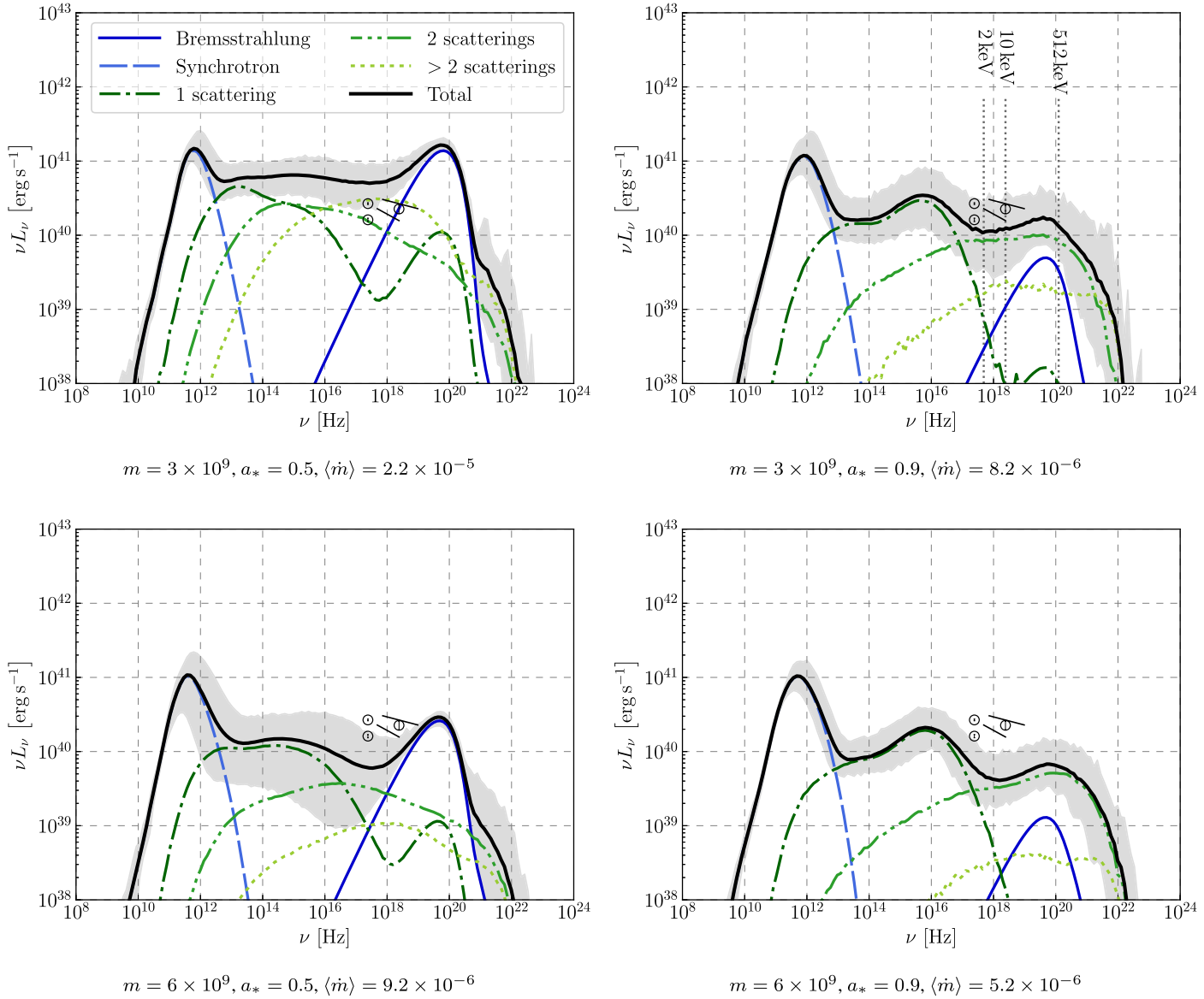

Figure 3. Time-averaged computed spectral energy distributions (SEDs) for the M87* models. The shaded region around the total SED shows the variability throughout the time-averaging period ($600GM/c^3$–$1000GM/c^3$). X-ray observations (Di Matteo et al. 2003; Prieto et al. 2016) are shown as circles, and their uncertainties as error bars inside the circles. Observed SEDs in the 2–10 keV (Di Matteo et al. 2003) and 3–40 keV (Wong et al. 2017) ranges are shown as solid black lines. Conversion from Jy to νL_ν assumed isotropic emission and a distance $D = 16.7$ Mpc to M87*. The model with $m = 3 \times 10^9$ and $a_* = 0.5$ overproduces X-rays. Bremsstrahlung dominates near $\nu \sim 10^{20}$ Hz when $a_* = 0.5$, and inverse Compton scattering dominates when $a_* = 0.9375$.

diagnostic of black hole spin. However, a significant part of the accretion disk in these simulations might not be in radiative and/or viscous equilibrium, so 3D studies are needed to know if this result is valid. Furthermore, the relationship between inverse Compton scattering and bremsstrahlung might depend on the magnetic field structure. We use simulations of SANE accretion disks, as opposed to magnetically arrested disks (MADs; Narayan et al. 2003); the latter have also been used to study M87* (Chael et al. 2019; Event Horizon Telescope Collaboration et al. 2019b).

Fits to X-ray observations of M87* provide an upper limit for the 2–10 keV luminosity of 5×10^{40} erg s^{-1} (Böhringer et al. 2001), 3.1×10^{40} erg s^{-1} (Di Matteo et al. 2003), and 4.4×10^{40} erg s^{-1} (Event Horizon Telescope Collaboration et al. 2019b). The average luminosity $\langle L_X \rangle$ of the model with $m = 3 \times 10^9$ and $a_* = 0.5$ is a factor of ≈3 larger than observations. Accounting for variability, $\langle L_X \rangle - 2\sigma_{L_X} = 3 \times 10^{40}$ erg s^{-1} is only marginally consistent. The fact that the observations encompass a larger part of the accretion flow and potentially unresolved sources strongly suggests this model is inconsistent with observations, as found in previous work (Ryan et al. 2018). The other models are less than an order of magnitude below this limit.

In our GRMHD models of Sgr A* we find that at fixed T_p/T_e and accretion rate bremsstrahlung becomes increasingly important compared to inverse Compton scattering as the viewing angle increases. The same trend holds at fixed viewing angle with increasing T_p/T_e. We hereafter focus on SEDs at a fixed viewing angle of $\sim\pi/3$ with respect to the black hole spin vector. These SEDs, shown in Figure 4, were computed by recording νL_ν for photons in an angular bin between 47° and 65°, corresponding to a solid angle Ω, and then multiplying these νL_ν by $4\pi/\Omega$. The 2–10 keV luminosities are $\{1.8, 0.43, 10\} \times 10^{33}$ erg s^{-1} for $T_p/T_e = \{1, 3, 10\}$, meaning the $T_p/T_e = 10$ model

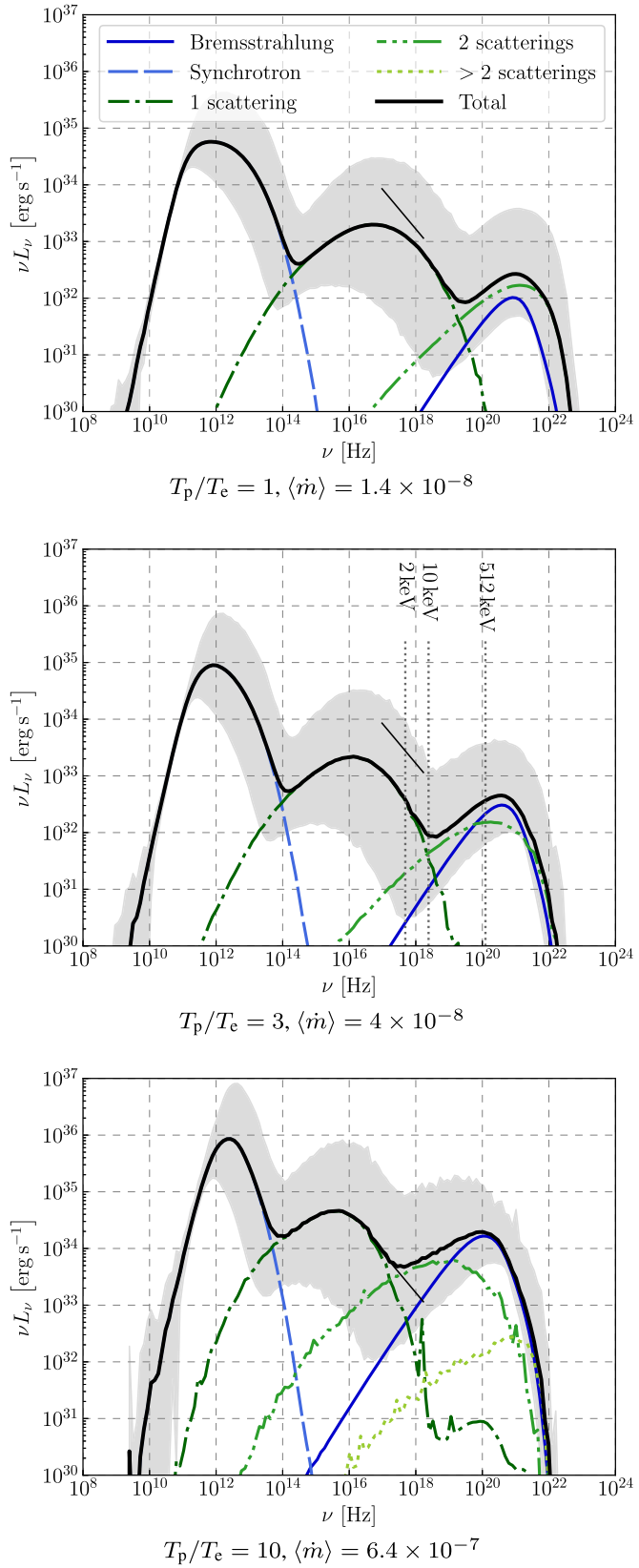

Figure 4. Time-averaged computed spectral energy distributions (SEDs) for Sgr A* ($m = 4.05 \times 10^6$, $a_* = 0.9375$) at a viewing angle of $\pi/3$. The shaded region around the total SED shows the variability throughout the time-averaging period. The SEDs are normalized to the observed 230 GHz flux (Doeleman et al. 2008).

overproduces compared to the observed values of 2.4×10^{33} erg s^{-1} (Baganoff et al. 2003) and 3.6×10^{33} erg s^{-1} (Nowak et al. 2012). At $T_p/T_e = 10$ bremsstrahlung dominates near $\nu \sim 10^{20}$ Hz, and at $T_p/T_e = 1$ double-scattered synchrotron photons dominate. In all models, synchrotron radiation dominates the total luminosity, while bremsstrahlung amounts to a $\lesssim$1% contribution.

4. Conclusion

We used the radiative transfer code `grmonty`, modified with a numerical bremsstrahlung prescription, to study bremsstrahlung in slowly accreting black holes as a function of accretion rate and spin. We found that bremsstrahlung is relatively constant in time and follows the expected scaling $\langle L^{\rm br} \rangle \propto \langle \dot{m} \rangle^2$ in the low-accretion rate regime. Bremsstrahlung contributes considerably to the SED near $\nu \sim 10^{20}$ Hz at all accretion rates, and to the total luminosity at $\dot{m} \approx 10^{-5}$. For M87*, we found that the $m = 3 \times 10^9$ and $a_* = 0.5$ model overproduces the observed 2–10 keV luminosity, and that X-ray variability might provide information about black hole spin, although 3D models are needed to fully explore this possibility.

This work is limited by axisymmetry of the RadGRMHD models and by the neglect of bremsstrahlung in the RadGRMHD evolutions themselves; in this sense the RadGRMHD calculation is not self-consistent. Possible future work includes (i) 3D RadGRMHD models that include bremsstrahlung self-consistently, (ii) using a nonthermal distribution of electrons, which is almost certainly required to produce the near-infrared flares in Sgr A*, and (iii) considering larger models and longer runs to model the emission from larger radii. While both bremsstrahlung and inverse Compton scattering produce photons with energy above the electron–positron pair production threshold, the optical depth to pair production remains $\lesssim 10^{-3}$ in all of our models.

We thank John Wardle for comments. We also thank the anonymous referee for a report that greatly improved the presentation of the paper. This work was supported by National Science Foundation (NSF) grants AST-1716327 and OISE-1743747. R.Y. was supported by NSF grants AST-1333612, AST-1716327, and OISE-1743747, as well as by a tuition and fee waiver from the University of Illinois at Urbana–Champaign. G.N.W. was supported by NSF grant AST-1716327 and by the US Department of Energy through Los Alamos National Laboratory. Los Alamos National Laboratory is operated by Triad National Security, LLC, for the National Nuclear Security Administration of the US Department of Energy (Contract No. 89233218CNA000001). This work has been assigned a document release number LA-UR-19-32704. This work used the Extreme Science and Engineering Discovery Environment (XSEDE) resource Stampede2 at the Texas Advanced Computing Center (TACC) through allocation TG-AST170024.

Software: `ebhlight` (Ryan et al. 2017), GNU Scientific Library, `grmonty` (Dolence et al. 2009), h5py, HDF5, Mathematica, Matplotlib (Hunter 2007), NumPy.

Appendix

Here we compare several bremsstrahlung emission coefficient formulae found in the literature. In general, the emission coefficient is not analytic and must be evaluated numerically. All formulae are simplified to the case of an ionized hydrogen plasma. The latter simplification might not be valid for Sgr A*, which is likely fueled by helium-rich stellar winds (Martins et al. 2007).

Appendix A
Electron–Ion Emission Coefficient

We consider four approximations for the electron–ion bremsstrahlung emission coefficient. The first three are of the form (e.g., Rybicki & Lightman 1979, 5.14a)

$$j_\nu^{\rm br,ei} = \frac{8\, q_{\rm e}^6}{3\, m_{\rm e}^2 c^4}\sqrt{\frac{2\pi}{3}}\,\Theta_{\rm e}^{-1/2} n_e n_i e^{-h\nu/\,k_{\rm B}\,T_{\rm e}}\bar{g}_{\rm ff}^{\rm ei}, \tag{A1}$$

where $q_{\rm e} \equiv$ electron charge, $m_{\rm e} \equiv$ electron mass, $c \equiv$ speed of light, $k_{\rm B} \equiv$ Boltzmann constant, $T_{\rm e} \equiv$ electron temperature, $\Theta_{\rm e} \equiv k_{\rm B}\,T_{\rm e}/\,m_{\rm e}c^2$, $n_{\rm e} \equiv$ electron number density, and $h \equiv$ Planck's constant. The thermally averaged electron–ion Gaunt factor is $\bar{g}_{\rm ff}^{\rm ei}$. The three approximations based on this form of the emission coefficient differ in their treatment of $\bar{g}_{\rm ff}^{\rm ei}$.

In the first approximation, the Gaunt factor is constant:

$$\bar{g}_{\rm ff}^{\rm ei} = 1.2. \tag{A2}$$

In the second approximation ("RL piecewise"), the Gaunt factor is given by a piecewise function (Novikov & Thorne 1973), which for $T_{\rm e} \gtrsim 10^5$ K is

$$\bar{g}_{\rm ff}^{\rm ei} = \begin{cases} \left(\frac{3}{\pi}\frac{k_{\rm B}\,T_{\rm e}}{h\nu}\right)^{1/2} & \frac{k_{\rm B}\,T_{\rm e}}{h\nu} < 1 \\ \frac{\sqrt{3}}{\pi}\ln\left(\frac{4}{\xi}\frac{k_{\rm B}\,T_{\rm e}}{h\nu}\right) & \frac{k_{\rm B}\,T_{\rm e}}{h\nu} > 1. \end{cases} \tag{A3}$$

Here $\xi \equiv \exp(\gamma_{\rm E}) \approx 1.781$, where $\gamma_{\rm E}$ is the Euler–Mascheroni constant.

In the third approximation ("RL van Hoof"), the Gaunt factor is computed numerically (van Hoof et al. 2015).

The fourth, distinct approximation ("Svensson EI") begins with a piecewise bremsstrahlung cooling rate (Svensson 1982), with small corrections (Narayan & Yi 1995) to ensure continuity across $\Theta_{\rm e} = 1$. An approximate emission coefficient follows from multiplying the cooling rate by $\bar{g}_{\rm ff}^{\rm ei} e^{-h\nu/\,k_{\rm B}\,T_{\rm e}} h/(4\pi\,k_{\rm B}\,T_{\rm e})$ (e.g., Straub et al. 2012):

$$j_\nu^{\rm br,ei} = \frac{4\,\pi\,q_{\rm e}^6}{3\,m_{\rm e}^2 c^4} F_{\rm ei}(\,\Theta_{\rm e})\,\Theta_{\rm e}^{-1}\,n_{\rm e}\,n_{\rm i} e^{-h\nu/\,k_{\rm B}\,T_{\rm e}}\bar{g}_{\rm ff}^{\rm ei},$$

$$F_{\rm ei}(\,\Theta_{\rm e}) = \begin{cases} 4\left(\frac{2\,\Theta_{\rm e}}{\pi^3}\right)^{1/2}(1 + 1.781\,\Theta_{\rm e}^{1.34}) & \Theta_{\rm e} < 1 \\ \frac{9\,\Theta_{\rm e}}{2\pi}[\ln(2\eta\,\Theta_{\rm e} + 0.48) + 1.5] & \Theta_{\rm e} > 1, \end{cases} \tag{A4}$$

where $\eta \equiv \exp(-\gamma_{\rm E}) \approx 0.561$.

Appendix B
Electron–Electron Emission Coefficient

A first approximation ("Svensson EE") is obtained using the same procedure to convert an electron–electron cooling rate from Svensson (1982) to an emission coefficient as in (A4), yielding

$$j_\nu^{\rm br,ee} = \frac{q_{\rm e}^6}{2\,m_{\rm e}^2 c^4} F_{\rm ee}(\,\Theta_{\rm e})\,\Theta_{\rm e}^{-1}\,n_{\rm e}^2 e^{-h\nu/\,k_{\rm B}\,T_{\rm e}}\bar{g}_{\rm ff}^{\rm ee},$$

$$F_{\rm ee}(\,\Theta_{\rm e}) = \begin{cases} \frac{20(44 - 3\pi^2)}{9\pi^{1/2}}\,\Theta_{\rm e}^{3/2} \\ \times\,(1 + 1.1\,\Theta_{\rm e} + \Theta_{\rm e}^2 - 1.25\,\Theta_{\rm e}^{5/2}) & \Theta_{\rm e} < 1 \\ 24\,\Theta_{\rm e}[\ln(2\eta\,\Theta_{\rm e}) + 1.28] & \Theta_{\rm e} > 1. \end{cases} \tag{B5}$$

Similarly, $\bar{g}_{\rm ff}^{\rm ee}$ is the thermally averaged electron–electron Gaunt factor. Another form of the emission coefficient ("Nozawa," Nozawa et al. 2009) is

$$j_\nu^{\rm br,ee} = \frac{4\pi\,q_{\rm e}^6}{3\,m_{\rm e}^2 c^4}\,\Theta_{\rm e}^{1/2}\,n_{\rm e}^2 e^{-h\nu/\,k_{\rm B}\,T_{\rm e}}\bar{g}_{\rm ff}^{\rm ee}, \tag{B6}$$

where $\bar{g}_{\rm ff}^{\rm ee}$ is given by an analytic fitting formula to numerical calculations (Nozawa et al. 2009).

Appendix C
Total Emission Coefficient

An approximation for the total emission coefficient can be constructed via multiplying the cooling rate presented in Equation (5).25 of Rybicki & Lightman (1979) by $e^{-h\nu/\,k_{\rm B}\,T_{\rm e}} h/(4\pi\,k_{\rm B}\,T_{\rm e})$ and setting $\bar{g}_{\rm B} = 1.2$, yielding

$$j_\nu^{\rm br} = \frac{8\,q_{\rm e}^6}{3\,m_{\rm e}^2 c^4}\sqrt{\frac{2\pi}{3}}\,\Theta_{\rm e}^{-1/2} n_e n_i e^{-h\nu/\,k_{\rm B}\,T_{\rm e}}\bar{g}_{\rm B}(1 + 2.61\,\Theta_{\rm e}). \tag{C7}$$

The extra factor (compared to Equation (A1)) accounts for electron–electron bremsstrahlung and relativistic effects (Novikov & Thorne 1973).

Appendix D
Comparison

We compare several approximate bremsstrahlung emission coefficients by computing their errors with respect to a reference emission coefficient. We choose this reference to be, for electron–ion bremsstrahlung, the emission coefficient (A1) with the van Hoof et al. (2015) Gaunt factor, since they compute the Gaunt factor numerically in the relativistic regime using the Born approximation and combine the results with a previous calculation in the nonrelativistic regime (van Hoof et al. 2014), thus spanning a large parameter space with high accuracy. For electron–electron bremsstrahlung, we choose the emission coefficient and Gaunt factor from Nozawa et al. (2009) as the reference calculation because, similarly, they merge nonrelativistic results with calculations that account for Coulomb corrections and relativistic effects when important.

We find that Equation (A1) using Equation (A2) underestimates the emission by more than an order of magnitude when $\Theta_{\rm e} > 1$ and $\nu > 10^{16}$ Hz, confirming the importance of electron–electron bremsstrahlung and relativistic effects in this

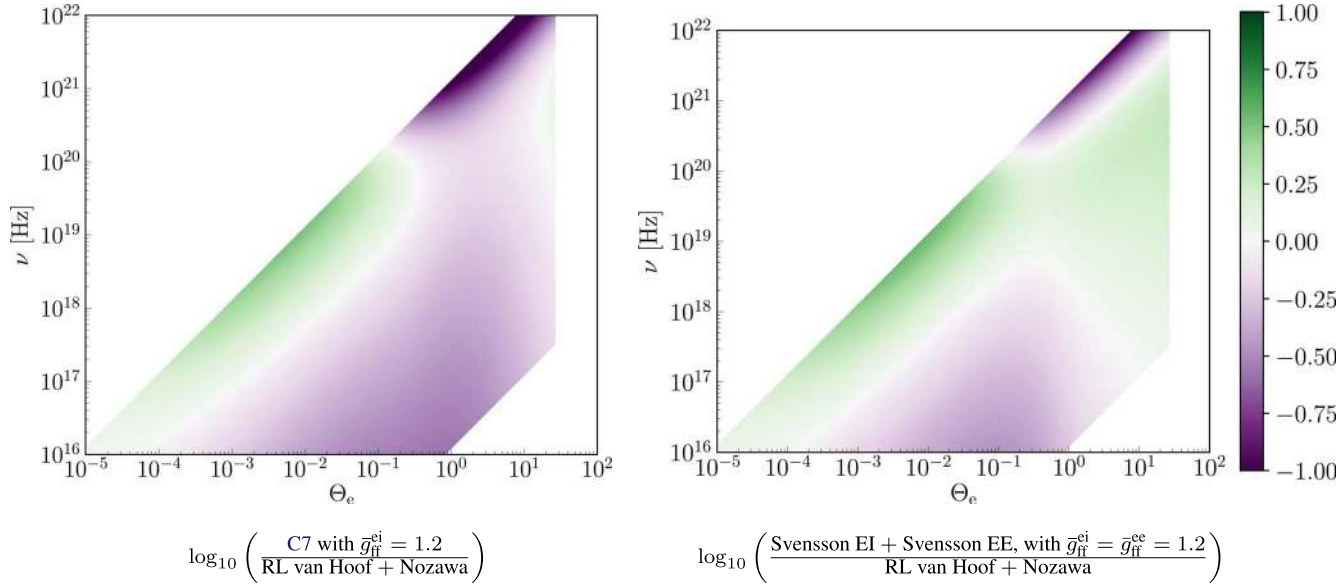

Figure D1. Error for some approximations of the emission coefficient as a function of frequency and dimensionless electron temperature when compared to the reference calculation, taken to be the sum of Equation (A1) with the van Hoof et al. (2015) Gaunt factor (electron–ion contribution) and Equation (B6) with the Nozawa et al. (2009) Gaunt factor (electron–electron contribution). The left panel shows the error for Equation (C7) using $\bar{g}_{\rm B}=1.2$. The right panel shows the error for Equation (A4) for electron–ion bremsstrahlung and (B5) for electron–electron bremsstrahlung, and $\bar{g}_{\rm ff}^{\rm ei}=\bar{g}_{\rm ff}^{\rm ee}=1.2$. The shape of the plotted region reflects the domain of validity of the reference calculation.

regime. We therefore focus on formulae that include both of these. To compare these fomulæ in the most application-agnostic way possible, we directly plot their errors as a function of frequency and temperature (Figure D1). The left panel shows the error for Equation (C7) with the constant Gaunt factor (A2). This approximation is within one order of magnitude of the reference calculation everywhere except at very high temperatures and frequencies. However, it consistently underestimates the emission by a factor of $\sim$2. The right panel shows the error for the sum of Equations (A4) and (B5), with $\bar{g}_{\rm ff}^{\rm ei}=\bar{g}_{\rm ff}^{\rm ee}=1.2$. This approximation has a smaller mean error and stays within one order of magnitude of the reference calculation everywhere. For these approximations, a constant Gaunt factor gives slightly better results than a piecewise Gaunt factor.

For applications to black hole accretion in which bremsstrahlung formulae are the leading source of error (and we do not know of any) we recommend the RL van Hoof + Nozawa formulae, although they are more computationally expensive and it would then be necessary to also account for helium abundance and metallicity, which we have not done here.

ORCID iDs

Ricardo Yarza https://orcid.org/0000-0003-0381-1039
George N. Wong https://orcid.org/0000-0001-6952-2147
Benjamin R. Ryan https://orcid.org/0000-0001-8939-4461
Charles F. Gammie https://orcid.org/0000-0001-7451-8935

References

Baganoff, F. K., Maeda, Y., Morris, M., et al. 2003, ApJ, 591, 891
Bélanger, G., Goldwurm, A., Renaud, M., et al. 2006, ApJ, 636, 275
Bird, S., Harris, W. E., Blakeslee, J. P., & Flynn, C. 2010, A&A, 524, A71
Blakeslee, J. P., Jordán, A., Mei, S., et al. 2009, ApJ, 694, 556
Boehle, A., Ghez, A. M., Schödel, R., et al. 2016, ApJ, 830, 17
Böhringer, H., Belsole, E., Kennea, J., et al. 2001, A&A, 365, L181
Cantiello, M., Blakeslee, J. P., Ferrarese, L., et al. 2018, ApJ, 856, 126
Chael, A., Narayan, R., & Johnson, M. D. 2019, MNRAS, 486, 2873
Di Matteo, T., Allen, S. W., Fabian, A. C., Wilson, A. S., & Young, A. J. 2003, ApJ, 582, 133
Dibi, S., Drappeau, S., Fragile, P. C., Markoff, S., & Dexter, J. 2012, MNRAS, 426, 1928
Doeleman, S. S., Fish, V. L., Schenck, D. E., et al. 2012, Sci, 338, 355
Doeleman, S. S., Weintroub, J., Rogers, A. E. E., et al. 2008, Natur, 455, 78
Dolence, J. C., Gammie, C. F., Mościbrodzka, M., & Leung, P. K. 2009, ApJS, 184, 387
Esin, A. A., Narayan, R., Ostriker, E., & Yi, I. 1996, ApJ, 465, 312
Event Horizon Telescope Collaboration, Akiyama, K., Alberdi, A., et al. 2019a, ApJL, 875, L1
Event Horizon Telescope Collaboration, Akiyama, K., Alberdi, A., et al. 2019b, ApJL, 875, L5
Event Horizon Telescope Collaboration, Akiyama, K., Alberdi, A., et al. 2019c, ApJL, 875, L6
Ford, A. L., Keenan, B. D., & Medvedev, M. V. 2018, PhRvD, 98, 063016
Gammie, C. F., McKinney, J. C., & Tóth, G. 2003, ApJ, 589, 444
Gebhardt, K., Adams, J., Richstone, D., et al. 2011, ApJ, 729, 119
Goldreich, P., & Julian, W. H. 1969, ApJ, 157, 869
Gravity Collaboration, Abuter, R., Amorim, A., et al. 2019, A&A, 625, L10
Howes, G. G. 2010, MNRAS, 409, L104
Hunter, J. D. 2007, CSE, 9, 90
Itoh, N., Kawana, Y., & Nozawa, S. 2002, NCimB, 117, 359
Mahadevan, R. 1997, ApJ, 477, 585
Marrone, D. P., Moran, J. M., Zhao, J.-H., & Rao, R. 2006, JPhCS, 54, 354
Martins, F., Genzel, R., Hillier, D. J., et al. 2007, A&A, 468, 233
Mościbrodzka, M., Gammie, C. F., Dolence, J. C., & Shiokawa, H. 2011, ApJ, 735, 9
Mościbrodzka, M., Gammie, C. F., Dolence, J. C., Shiokawa, H., & Leung, P. K. 2009, ApJ, 706, 497
Narayan, R., Igumenshchev, I. V., & Abramowicz, M. A. 2003, PASJ, 55, L69
Narayan, R., Sądowski, A., Penna, R. F., & Kulkarni, A. K. 2012, MNRAS, 426, 3241
Narayan, R., & Yi, I. 1995, ApJ, 452, 710
Novikov, I. D., & Thorne, K. S. 1973, in Black Holes (Les Astres Occlus), ed. C. DeWitt & B. DeWitt (New York: Gordon and Breach), 343
Nowak, M. A., Neilsen, J., Markoff, S. B., et al. 2012, ApJ, 759, 95
Nozawa, S., Takahashi, K., Kohyama, Y., & Itoh, N. 2009, A&A, 499, 661
Parfrey, K., Philippov, A., & Cerutti, B. 2019, PhRvL, 122, 035101
Prieto, M. A., Fernández-Ontiveros, J. A., Markoff, S., Espada, D., & González-Martín, O. 2016, MNRAS, 457, 3801
Ressler, S. M., Tchekhovskoy, A., Quataert, E., Chandra, M., & Gammie, C. F. 2015, MNRAS, 454, 1848
Ryan, B. R., Dolence, J. C., & Gammie, C. F. 2015, ApJ, 807, 31

Ryan, B. R., Ressler, S. M., Dolence, J. C., et al. 2017, ApJL, 844, L24
Ryan, B. R., Ressler, S. M., Dolence, J. C., Gammie, C., & Quataert, E. 2018, ApJ, 864, 126
Rybicki, G. B., & Lightman, A. P. 1979, Radiative Processes in Astrophysics (New York: Wiley-Interscience)
Sądowski, A., Narayan, R., McKinney, J. C., & Tchekhovskoy, A. 2014, MNRAS, 439, 503
Stepney, S., & Guilbert, P. W. 1983, MNRAS, 204, 1269
Straub, O., Vincent, F. H., Abramowicz, M. A., Gourgoulhon, E., & Paumard, T. 2012, A&A, 543, A83
Svensson, R. 1982, ApJ, 258, 335
van Hoof, P. A. M., Ferland, G. J., Williams, R. J. R., et al. 2015, MNRAS, 449, 2112
van Hoof, P. A. M., Williams, R. J. R., Volk, K., et al. 2014, MNRAS, 444, 420
Walsh, J. L., Barth, A. J., Ho, L. C., & Sarzi, M. 2013, ApJ, 770, 86
Wilson, A. S., & Yang, Y. 2002, ApJ, 568, 133
Wong, K.-W., Nemmen, R. S., Irwin, J. A., & Lin, D. 2017, ApJL, 849, L17
Yuan, F., & Narayan, R. 2014, ARA&A, 52, 529